

# A white light confocal microscope for spectrally resolved multidimensional imaging

J. H. FRANK\*, A. D. ELDER†, J. SWARTLING‡,  
A. R. VENKITARAMAN‡, A. D. JEYASEKHARAN‡  
& C. F. KAMINSKI†

\*Combustion Research Facility, Sandia National Laboratories, Livermore, CA 94611, USA

†Department of Chemical Engineering, University of Cambridge, Cambridge, UK

‡MRC Cancer Cell Unit, Hutchinson/MRC Research Centre, Cambridge, UK

**Key words.** Confocal microscopy, fluorescence microscopy, photonic crystal fibre, supercontinuum.

## Summary

Spectrofluorometric imaging microscopy is demonstrated in a confocal microscope using a supercontinuum laser as an excitation source and a custom-built prism spectrometer for detection. This microscope system provides confocal imaging with spectrally resolved fluorescence excitation and detection from 450 to 700 nm. The supercontinuum laser provides a broad spectrum light source and is coupled with an acousto-optic tunable filter to provide continuously tunable fluorescence excitation with a 1-nm bandwidth. Eight different excitation wavelengths can be simultaneously selected. The prism spectrometer provides spectrally resolved detection with sensitivity comparable to a standard confocal system. This new microscope system enables optimal access to a multitude of fluorophores and provides fluorescence excitation and emission spectra for each location in a 3D confocal image. The speed of the spectral scans is suitable for spectrofluorometric imaging of live cells. Effects of chromatic aberration are modest and do not significantly limit the spatial resolution of the confocal measurements.

## Introduction

Confocal fluorescence microscopy is one of the most powerful techniques for probing a wide range of phenomena in biological sciences (Pawley, 1995). The photophysical properties of a fluorophore are affected by interactions of the fluorophore with its local environment, resulting in variations of fluorescence intensity, lifetime, anisotropy, and emission and excitation spectra. These interactions represent opportunities for sensitive probing of local environmental properties,

such as pH, viscosity, and the presence of quenchers, and enable detection of phenomena, such as binding events or conformational changes in macromolecules.

The applications of fluorescence microscopy are rapidly expanding as scientists probe increasingly complex and varied biological systems. These applications require advances in microscopy technology. Developments of new fluorophores are significantly enhancing labelling specificity and providing new opportunities for studying complex phenomena using simultaneous measurements of multiple different fluorophores. Advancements in microscope instrumentation are required to implement these multiplexed fluorophore measurements and to provide a more complete characterization of the interactions of fluorophores with their local environment.

The demand for more sophisticated and versatile microscopy systems requires innovative coupling of microscopes with advanced laser and detector technologies. These technologies can provide unprecedented detection sensitivity and flexibility for fluorescence measurements. Until recently, the inability to arbitrarily choose fluorescence excitation, and detection wavelengths and bandwidths presented a bottleneck in the advancement of confocal laser scanning microscopy (CLSM). Currently, most commercial confocal systems use a combination of lasers to excite fluorescence at a small number of discrete wavelengths in the visible spectrum. However, flexibility in wavelength selection is essential for optimal excitation and detection of fluorophores (Zimmermann *et al.*, 2003).

Full flexibility in targeting any wavelength interval in the visible spectrum enables simultaneous measurements of different species, structures and phenomena using multiplexed detection of several fluorophores (Stephens *et al.*, 2000). The ability to rapidly change between any

Correspondence to: Jonathan H. Frank. Tel: +1 925 294 4645; fax: +1 925 294 2595; e-mail: jhfrank@sandia.gov; cfk23@cam.ac.uk

visible excitation wavelength greatly enhances the use of photo-activated dyes (Lippincott-Schwartz *et al.*, 2003; Betzig *et al.*, 2006). Spectrally resolved fluorescence measurements are essential for differentiating multiple fluorophore signals from one another and from interferences, such as autofluorescence. The spectral differentiation of autofluorescence signals enables entirely new diagnostic opportunities. For example, measurements at multiple excitation and emission wavelengths may significantly enhance the use of autofluorescence as a diagnostic tool for applications such as *in vivo* differentiation of healthy and diseased tissue. This approach would provide image contrast without requirements for labelling (Zellweger *et al.*, 2001). A similar image contrasting capability has been demonstrated with fluorescence lifetime imaging (Tadrous *et al.*, 2003).

Currently, the most commonly used excitation sources for CLSM systems are gas lasers, such as Ar-ion or He-Ne lasers, and diode lasers for operation in the visible to near-UV spectral regions. For emission detection, photomultiplier tubes (PMT) are normally used in conjunction with dichroic mirrors and bandpass filters for spectral selection. These configurations create spectrally inflexible systems, and only recently have solutions emerged to address these problems.

For fluorescence excitation, novel laser sources that generate white light supercontinua show excellent potential for CLSM imaging applications. For microscopy applications, supercontinua are usually generated by pumping a photonic crystal fibre (PCF; Dudley *et al.*, 2006) or a tapered silica fibre with ultrashort pulses from a Ti:sapphire laser (Dunsby *et al.*, 2004; McConnell, 2004; Betz *et al.*, 2005; Palero *et al.*, 2005). Once a supercontinuum is generated, the desired excitation wavelength must be selected. Techniques for wavelength selection include bandpass filters (McConnell, 2004), spatial dispersion of the supercontinuum with a prism (Dunsby *et al.*, 2004), acousto-optic beam splitters (AOBS; Betz *et al.*, 2005) and acousto-optic tunable filters (AOTF; Borlinghaus *et al.*, 2006). The use of bandpass filters is straightforward to implement but inflexible. Spatial dispersion of the beam using a prism can lead to large losses and does not allow simultaneous excitation with multiple excitation lines. The AOTF is a well-established technology that provides computer-controlled multiline wavelength selection over a broad spectral range.

For emission detection, a grating (Schultz *et al.*, 2001) or prism (Frederix *et al.*, 2001) is used to spatially disperse the different emission wavelengths, and the dispersed spectrum is imaged onto an array detector (Sinclair *et al.*, 2006). The array detector provides rapid acquisition of an entire emission spectrum but may limit the detection sensitivity in low-signal applications. An alternative approach is to pass the spatially dispersed emission through an adjustable slit system and onto a PMT. The emission spectra are measured sequentially by scanning the slit position. Although this approach is slower than the array detector, it provides flexibility for improving

the detection limit in low-signal applications by increasing the bandwidth of the detection (Borlinghaus *et al.*, 2006). For specialized CLSM applications, simultaneous time- and wavelength-resolved detection is possible with time- and position-sensitive detector systems (Plessow *et al.*, 2000; Luong *et al.*, 2005).

Here we describe the design and first full calibration of a confocal microscope system with continuously tunable fluorescence excitation and emission wavelengths and bandwidths. This system has the flexibility for optimal excitation and detection of a wide range of fluorophores and provides a new capability for multiparameter fluorescence measurements. Previous work has shown the potential of multiparameter fluorescence as an analytical tool (Borlinghaus *et al.*, 2006). The excitation and detection systems are fully integrated into a commercial confocal microscope while retaining all of its intrinsic features, such as three-dimensional (3D) imaging, frame and line averaging, and region-of-interest scanning. For an excitation source, we use a compact fibre-laser pumped PCF that generates supercontinuum radiation. This laser technology is a promising alternative to the more complex and expensive Ti:sapphire-based supercontinuum systems. For spectrally resolved detection, we use a custom-designed prism spectrometer with a computer-controlled slit mechanism. The spectral and spatial resolutions of the system are assessed. The integrated microscope system is optimized for light throughput and has sensitivity and spatial resolution that is comparable to top-of-the-range commercial CLSM systems. We demonstrate high-resolution spectrofluorometric measurements with voxel sizes of less than 0.1 femtoliters.

## Experimental methods

The spectrofluorometric imaging system is constructed around a commercial confocal microscope scanning unit (Olympus FluoView 300) coupled with an Olympus IX70 inverted microscope frame (Olympus UK, Southall, UK). All lasers are removed from the original CLSM frame, and the unit is modified to accept an external light source for fluorescence excitation. A fibre optic signal collection system has been designed to transmit signals from the confocal pinhole to the spectrograph for detection. A schematic diagram of the integrated system is shown in Fig. 1. The excitation, detection and image acquisition are fully computer controlled. The confocal scanning and image acquisition are controlled with Olympus' proprietary software (FluoView ver. 4.3 with TIEMPO) (Olympus UK, Southall, UK) on one computer. A second computer controls the fluorescence excitation and detection wavelengths with a custom-designed LabView (National Instruments UK, Newbury, UK) application. For performing fluorescence excitation and emission scans, the excitation, detection and confocal subsystems are synchronized by sending triggering signals between the two computers.

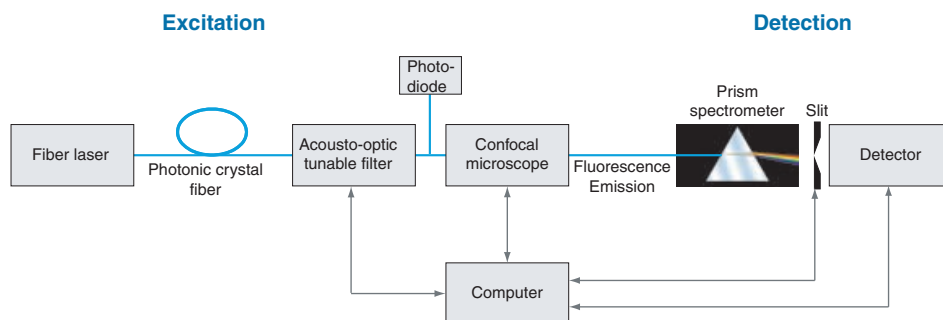


Fig. 1. Experimental configuration of multispectral confocal imaging microscope.

The output from a supercontinuum laser (Fianium SC450, Fianium, Southampton, UK) is passed through an AOTF to provide continuously tunable fluorescence excitation throughout the visible spectrum. The full spectrum of the supercontinuum laser spans 450–1700 nm with a total output power of 4 W. In the present configuration, the infrared radiation is removed from the beam by dichroic mirrors, and only the visible portion of the spectrum is used. The supercontinuum laser system produces approximately 5-ps pulses at 40 MHz and consists of a master laser, an amplifier and a PCF. The low-power master laser is a passively mode locked Yb-doped core-pumped fibre laser ( $\lambda = 1060$  nm). The master laser is coupled to a high-power cladding-pumped fibre amplifier. The amplified output pumps a high nonlinearity PCF, which generates a broad spectrum of spatially coherent light by a combination of nonlinear optical effects and anomalous group velocity dispersion (Dudley *et al.*, 2006). Nonlinear effects, such as self-modulation, cross-modulation, four-wave mixing and stimulated Raman scattering, are induced by intense laser light that is confined to the small-diameter core of the microstructured fibre. Figure 2a shows the visible region of the PCF-generated spectrum with different pump powers. The pump power is varied by adjusting the fibre amplifier gain. At low powers, only the red portion of the spectrum is present. As the power is increased, the shorter wavelength regions of the spectrum fill in. At maximum

power, a prominent peak appears at approximately 480 nm, and a minor isolated peak emerges at 432 nm.

The AOTF filter provides a continuously adjustable bandpass filter that selects lines from the supercontinuum spectrum. As many as eight bands can be selected simultaneously with each band having approximately a 1-nm bandwidth. The intensity and the centre wavelength of each band can be independently controlled by changing the acoustic power and modulation frequency, respectively. The bandpass can be tuned from 450 to 700 nm by varying the AOTF modulation frequency from 80 to 150 MHz. The AOTF driver is computer controlled via an RS-232 serial connection using LabView. Figure 2b shows a power spectrum that was measured by tuning a single transmission band of the AOTF from 450 to 650 nm. This spectrum was recorded with the fibre amplifier at maximum power. If additional power is required, multiple closely spaced bandpasses can provide significantly greater than 1 mW total power at any visible wavelength. Figure 3 illustrates the multiline capabilities of the AOTF with a spectrum that was produced by programming the AOTF to transmit two separate combs in the blue and green regions with four lines in each comb. The width of the individual transmission lines was less than or comparable to the 1–2 nm resolution of the spectrometer that was used to measure the spectrum (Ocean Optics USB2000, Ocean Optics, Dunedin, FL, USA). The minimum wavelength separation between two

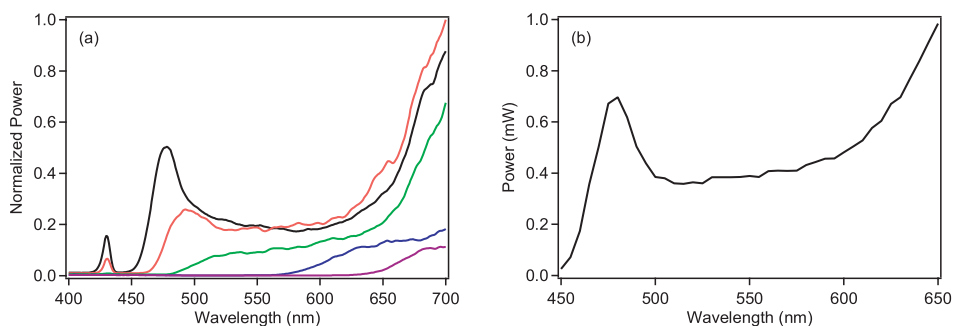


Fig. 2. (a) Visible portion of the supercontinuum spectrum generated by the photonic crystal fibre with different pumping powers. Black curve corresponds to the maximum laser power. (b) AOTF-transmitted power for a single line with full laser power.

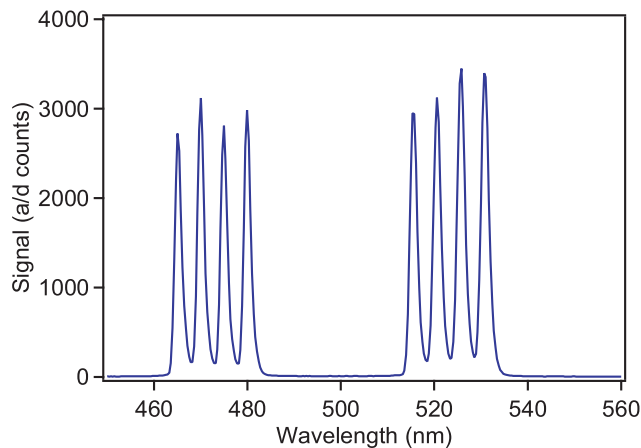


Fig. 3. Example of a multiline excitation spectrum using a programmable AOTF to simultaneously select eight different lines.

lines is limited by the minimum spacing of the corresponding acoustic modulation frequencies. The minimum separation of the modulation frequencies for two adjacent lines is approximately 500 kHz, which corresponds to 1–4 nm depending on the wavelength. For smaller line separations, the beating between the acoustic frequencies produces significant intensity fluctuations in the transmitted light, which can create stripes in the confocal images.

The multiline capability may provide sufficient peak intensities for two-photon fluorescence microscopy in some applications. The use of all eight AOTF lines provides approximately 8 mW of 5-ps pulses at 40 MHz in the red region, and this capability could be extended to the near infrared with a different AOTF. Many commercial two-photon microscopy systems use Ti:sapphire lasers with subpicosecond pulse durations and higher repetition rates (Denk *et al.*, 1995). Palero *et al.* (2005) demonstrated that two-photon fluorescence excitation is possible with supercontinua generated from a Ti:sapphire-pumped PCF. To compare our supercontinuum system with commercial Ti:sapphire systems, we consider the parameters that govern the two-photon laser-induced fluorescence (LIF) signal. For a fixed pixel dwell time, the two-photon LIF signal is proportional to  $P_{\text{peak}}^2 f \tau$ , or equivalently to  $\bar{P}^2 / f \tau$ , where  $P_{\text{peak}}$  and  $\bar{P}$  are the peak and average laser powers, respectively,  $f$  is the pulse repetition rate and  $\tau$  is the pulse width. Using this relationship, we estimate that two-photon LIF excitation with  $\bar{P} = 8$  mW from the supercontinuum laser would produce a LIF signal that is comparable to excitation with  $\bar{P} = 2.5$  mW from a Ti:sapphire laser with 250-fs pulses and a repetition rate of 80 MHz. For some applications, this power is sufficient for two-photon LIF imaging, whereas other applications require larger powers (Konig, 2000; Diaspro *et al.*, 2001). Note that the actual two-photon excitation efficiency will depend on a number of parameters, including the two-photon cross-section of the fluorophore, the temporal coherence of different wavelengths

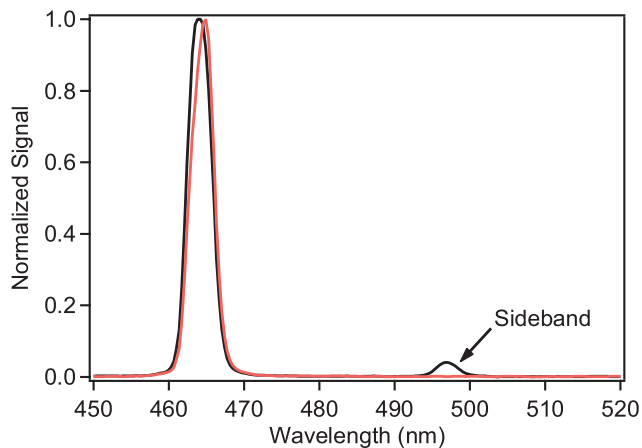


Fig. 4. Transmission spectrum from two different AOTF drivers with and without sideband transmission.

within the supercontinuum laser spectrum as well as the overlap of these wavelengths with the fluorophore's absorption spectrum.

The spectral purity of the transmitted light is another issue that must be considered when using an AOTF to filter a broadband light source. The narrow-band transmission spectrum of a single line can be degraded by the presence of sidebands that arise from the distribution of the acoustic field in the acousto-optic crystal. These sidebands can be particularly problematic if the output of the acousto-optic driver electronics contains excess frequency components. Sidebands can be significantly attenuated by using an additional AOTF, or a second pass through the same AOTF. Figure 4 shows the transmission spectrum for a bandpass centered at 465 nm using two different AOTF drivers. One of the AOTF drivers produced a significant sideband that was offset from the main band by approximately 30 nm. This sideband was eliminated by a double-pass configuration that was implemented by retroreflecting the beam through the AOTF. The disadvantage of using a second pass is that the transmission of the primary line is reduced by approximately 50%. The second AOTF driver provided an improved acoustic spectrum and eliminated this sideband. In this case, a single pass through the AOTF was used with negligible contributions from sidebands.

The output beam from the AOTF is aligned onto the confocal scanning mirrors after being reflected by a 20/80 (R/T) broadband beamsplitter. In the present setup, the 20/80 beamsplitter replaces the excitation dichroic beamsplitter that is used in the standard configuration of the confocal microscope. The total throughput of the optical path for the excitation beam, including the objective lens, mirrors and the 20/80 beamsplitter, varied from 8–10% over the visible spectrum. The 20/80 beamsplitter was chosen to pass the maximum signal over the entire visible spectrum while minimizing nonlinear effects, such as photobleaching or saturation of the fluorophores. If nonlinear effects are

negligible and the fluorescence detection sensitivity is limited by the available laser intensity, the signal levels in the CLSM can be increased by approximately 56% by replacing the 20/80 beamsplitter with a 50/50 beamsplitter.

Fluorescence emission is detected using a high-efficiency prism spectrometer that is based on the design by Frederix *et al.* (Frederix *et al.*, 2001). The spectrometer is coupled to the confocal microscope using a multimode optical fibre (105  $\mu\text{m}$  core diameter, NA = 0.22). The microscope objective images the fluorescence from the sample onto the standard confocal aperture. The confocal aperture is imaged onto the input of the optical fibre using an antireflection (AR)-coated doublet achromat (f.l. = 20 mm) to minimize chromatic aberrations. Ray tracing software (Winlens 4.3, Linos Photonics, Milton Keynes, UK) was used to optimize the imaging of the pinhole onto the fibre by matching the numerical apertures of the imaging lens and the fibre. The output of the optical fibre is positioned at the focal point of the spectrometer objective lens (achromat, f.l. = 120 mm). The collimated light that emerges from the objective lens is dispersed by a 60-mm AR-coated equilateral SF10 prism. The dispersed spectrum is focused onto the spectrometer exit slit by the spectrometer imaging lens (achromat, f.l. = 80 mm). A sidewindow PMT (Hamamatsu R3896, Hamamatsu Photonics UK, Welwyn Garden City, UK) is positioned at the spectrometer exit slit. The imaging system is designed to yield a maximum spatial dispersion of 80 mm in the slit plane (see Fig. 5) to prevent overfilling of the active area of the detector. The exit slit system is custom built and consists of two knife edges mounted in a linear stage. The wavelength and bandwidth of the emission detection are controlled by positioning the knife edges using computer-controlled stepper motors. The slit width can be adjusted from 25  $\mu\text{m}$  to fully open (8 mm) with 25- $\mu\text{m}$  resolution using a digital counter card and control software from National Instruments.

The prism spectrometer design calculations are compared with measurements of the spectrometer's dispersion. For a

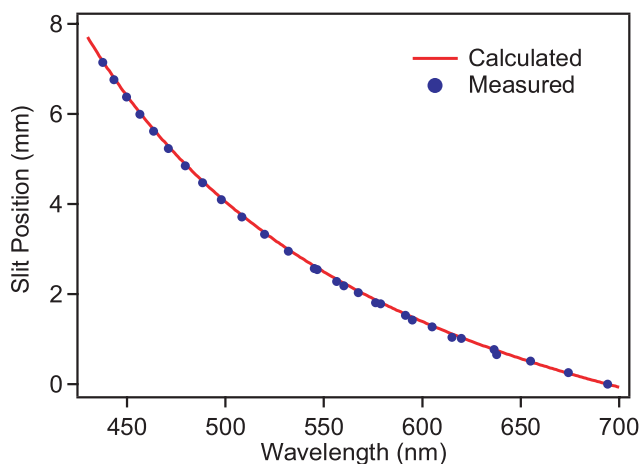


Fig. 5. Comparison of measured and calculated dispersion curves for prism spectrometer.

given spectral bandpass,  $\delta\lambda$ , the image size  $\Delta x$  in the slit plane varies as

$$\Delta x = f \frac{d\theta_D}{dn} \frac{dn}{d\lambda} \delta\lambda, \quad (1)$$

where  $f$  is the focal length of the spectrometer imaging lens (80 mm),  $\theta_D$  is the deviation angle and  $n$  the refractive index (Born & Wolf, 1980). The dispersion  $dn/d\lambda$  is calculated using Sellmeier's dispersion formula:

$$n^2(\lambda) - 1 = \frac{B_1\lambda^2}{\lambda^2 - C_1} + \frac{B_2\lambda^2}{\lambda^2 - C_2} + \frac{B_3\lambda^2}{\lambda^2 - C_3}, \quad (2)$$

where  $B_i$  and  $C_i$  are dispersion coefficients for SF10 (SCHOTT, 2006). The spectrometer is operated at a fixed input angle under minimum deviation (Klein & Furtak, 1986) at 543 nm, which corresponds to the wavelength of the helium neon laser that is used to align the spectrometer.

Figure 5 shows the excellent agreement between the computed and measured dispersion curves. The centre wavelength for each position of the slit is measured by illuminating a blank slide with a single line from the AOTF and detecting elastically scattered light while the AOTF wavelength is scanned. The theoretical spectral resolution of the spectrometer can be determined from the derivative of the dispersion curve. The dispersion of SF10 is larger at shorter wavelengths, and consequently the spectral resolution increases as the wavelength decreases. For example, a spectral bandpass of  $\delta\lambda = 1$  nm corresponds to slit sizes that vary approximately from  $\Delta x = 65$   $\mu\text{m}$  to 8  $\mu\text{m}$  at  $\lambda = 450$  and  $\lambda = 750$  nm, respectively. In practice, the spectral resolution is limited by the slit width and the diameter of the optical fibre at the input of the spectrometer. Figure 6 shows a calculation of the spectral resolution for fibre diameters from 50 to 300  $\mu\text{m}$ . The selection of the fibre diameter is a compromise between spectral resolution and detection sensitivity. The use of larger fibres improves the detection sensitivity by enabling more efficient coupling from the confocal aperture but decreases the

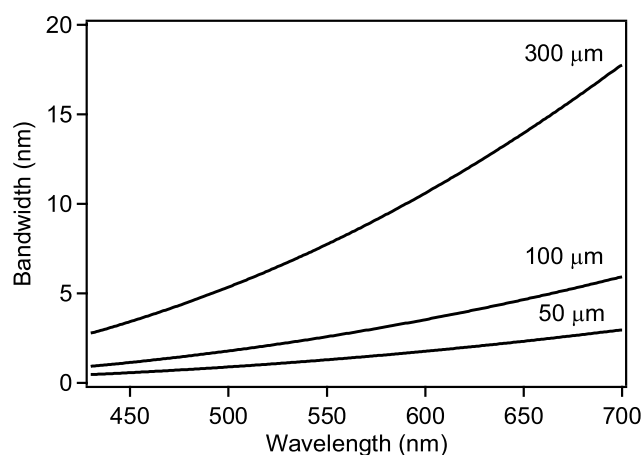


Fig. 6. Calculated spectrometer resolution for entrance slit widths of 50, 100 and 300  $\mu\text{m}$ .

spectral resolution. For the confocal images presented here, we use a 105  $\mu\text{m}$  fibre, which provides spectral resolutions of 1.5 nm for detection at 450 nm and 6 nm at 700 nm. The overall transmission of the spectrometer, including the 105  $\mu\text{m}$  fibre, was approximately 75% across the visible spectrum. The sensitivity of the spectrometer is thus better than or comparable to the standard confocal detector configuration, which requires the use of dichroic and bandpass filters to block background scattering. These filters can significantly reduce the detected signal, and a large set of filter combinations is required to optimize the detection sensitivity for different fluorophores.

## Results and discussion

### Characterization of fluorophores with fluorescence emission and excitation scans

*In situ* confocal imaging of fluorescence excitation and emission spectra are an important tool for characterizing fluorophores and using multiple fluorophores to label a sample. As a demonstration of this capability, we performed fluorescence excitation and emission scans of three dyes with the confocal microscope system. Figure 7 shows measured excitation and emission spectra of Rhodamine 6G, Rhodamine B and Coumarin 6 dyes, whose combined fluorescence spectra cover much of the visible spectrum. For these measurements, solutions of the dyes in ethanol were placed in multiwell plates on the microscope stage. The spectra measured with the confocal system are compared with absorption and emission spectra that were measured with a commercial spectrometer. The excellent agreement between these reference spectra and the spectra measured with the confocal system is evident in Fig. 7. These results demonstrate that precision spectrofluorometry can be performed at diffraction-limited resolution and that even subtle changes in absorption/emission features can be differentiated with this instrument. An exciting opportunity exists for identifying molecules from such spectral signatures without any requirement for labelling the sample.

Accurate spectral scans require careful corrections for variations in the excitation laser power, detection bandwidth and detector sensitivity. The scans presented here are corrected for these factors with the corrected fluorescence signal given by

$$S_{\text{corr}} = S_{\text{meas}} \frac{C}{P_{\text{laser}} T_{\text{exc}}(\lambda_{\text{exc}}) R_{\text{det}}(\lambda_{\text{det}}) T_{\text{det}}(\lambda_{\text{det}}) \Delta\lambda_{\text{det}}}, \quad (3)$$

where  $S_{\text{meas}}$  is the measured fluorescence signal,  $C$  is a calibration constant,  $P_{\text{laser}}$  is the laser power,  $\lambda_{\text{exc}}$  and  $\lambda_{\text{det}}$  are the excitation and detection wavelengths, respectively,  $T_{\text{exc}}(\lambda)$  is the total transmittance of the optical train that directs the laser beam to the sample,  $R_{\text{det}}(\lambda)$  is the detector sensitivity,  $T_{\text{det}}(\lambda)$  is the total transmittance of the detection optical train

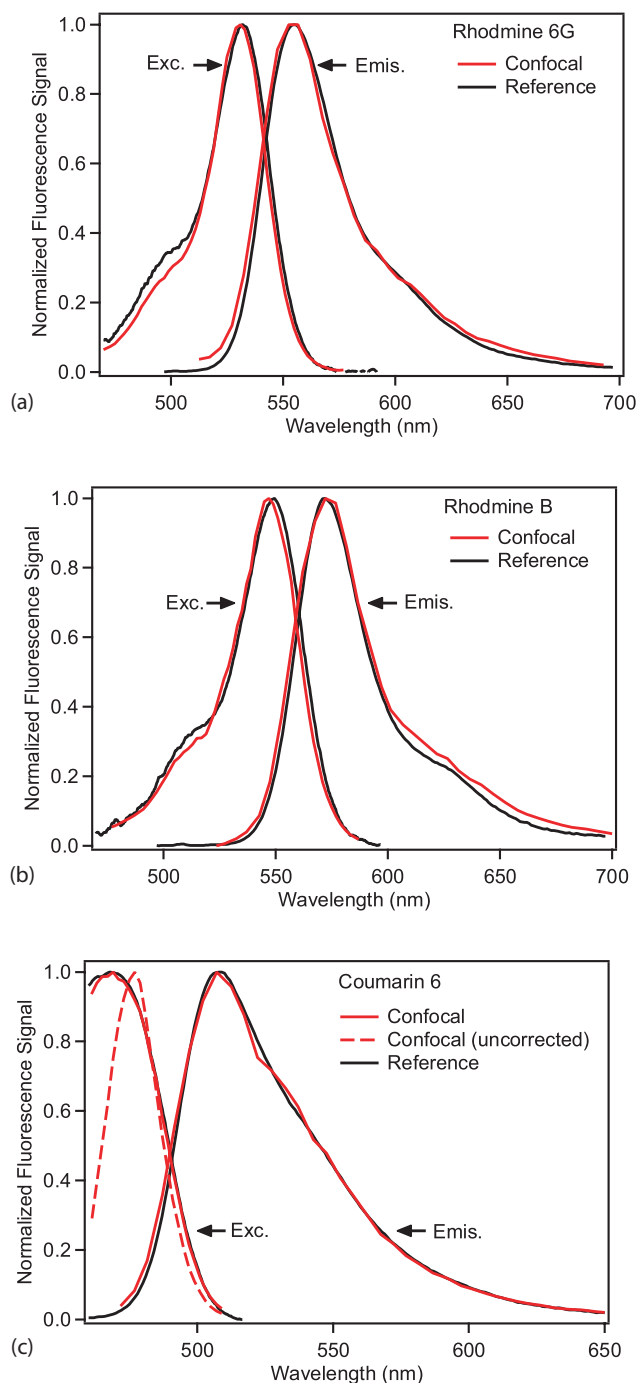
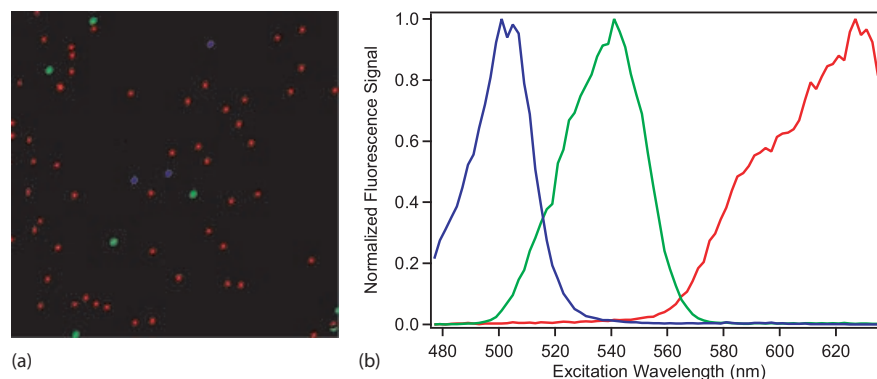


Fig. 7. Excitation and emission spectra of (a) Rhodamine 6G, (b) Rhodamine B, (c) Coumarin 6 measured with the multispectral confocal microscope. Results are compared with reference absorption and emission spectra measured using a commercial spectrometer.

and  $\Delta\lambda_{\text{det}}$  is the detection bandwidth of the spectrometer. Equation (3) is valid for narrow detection bandwidths for which the product  $R_{\text{det}}(\lambda)T_{\text{det}}(\lambda)$  is approximately constant. These corrections are particularly important for scans that cover a large range of wavelengths. As an illustration of the



**Fig. 8.** (a) Confocal image of a mixture of microbeads containing three different fluorescent dyes. The different beads are identified by a fluorescence excitation scan and are displayed with corresponding blue, green and red colour palettes. (b) Fluorescence excitation spectra are depicted for the blue, green and red beads.

quality of the corrections in these dye spectra, we consider the Coumarin 6 excitation spectrum, which spans a range of the supercontinuum spectrum that includes a significant peak at 480 nm (see Fig. 2). The dashed line in Fig. 7c shows an excitation spectrum that was measured with the confocal system prior to the laser power correction. Despite the large variation in the excitation power, the corrected spectrum (solid line) shows excellent agreement with the reference spectrum. For the excitation scans presented here, the emission spectra remained relatively constant, allowing for broadband detection without corrections for variations in  $R_{\text{det}}(\lambda)T_{\text{det}}(\lambda)$ . However, corrections for variations in  $R_{\text{det}}(\lambda)T_{\text{det}}(\lambda)$  and the spectrometer detection bandwidth are required for scans of the emission spectra. In principle, it is possible to keep the detection bandwidth of the instrument constant during a spectral scan by adjusting the separation of the knife edges. For the scans shown in this paper, however, both stepper motors are moved at the same speed resulting in a constant slit width and a variable bandpass (see Fig. 6) for which the measured spectra are corrected using Eq. 3. The excellent agreement between the reference and corrected emission spectra in Fig. 7 illustrates this correction capability.

#### *Multiplexed fluorophore measurements*

The multiplexing capability of the confocal microscope system is illustrated by imaging a mixture of microbeads containing three different fluorescent dyes. The beads are 0.18- $\mu\text{m}$  diameter PS-Speck beads (Molecular Probes, Invitrogen, Carlsbad, CA, USA) with excitation and emission maxima at approximately 505/515 nm, 540/560 nm and 633/660 nm. A fluorescence excitation scan is performed using two-dimensional (2D) confocal imaging. At each excitation wavelength, a 29  $\mu\text{m} \times 29 \mu\text{m}$  region is imaged with a 60 $\times$  objective lens (Olympus PlanApo, N.A. 1.4/oil). The spectrometer slits are configured to operate as an adjustable longpass filter. At each excitation wavelength, the slits are

positioned such that the cutoff wavelength is 10 nm longer than the excitation wavelength. This approach optimizes the detection sensitivity while blocking elastic scattering at the excitation wavelength. Figure 8a displays a composite image of the mixture of beads. The blue, green and red beads were detected using fluorescence excitation at 508 nm, 560 nm and 632 nm, respectively. This result demonstrates the excellent contrast that an excitation scan can provide for a mixture of fluorophores. The measured excitation spectra for the different beads are plotted in Fig. 8b. Each spectrum is an average of three beads with the same colour. This ability to multiplex the detection of multiple fluorophores is a powerful tool that can provide simultaneous measurements of different phenomena in biological samples.

#### *Spatial resolution and chromatic aberrations*

A broad range of fluorescence excitation and detection wavelengths is used in this confocal microscope system, and it is important to consider chromatic aberrations and variations in spatial resolution with wavelength. To evaluate these issues, we compare the widths of the point spread functions (PSFs) in the blue and red spectral regions. The PSFs are determined from 3D confocal images of blue and red fluorescent subresolution microbeads (0.18- $\mu\text{m}$  diameter) using excitation wavelengths of 490 nm and 620 nm, respectively. Each 3D image contains 60–100 microbeads and is recorded with the same 60 $\times$  oil immersion lens as above and a 150- $\mu\text{m}$  confocal aperture. The dimensions of the images are 512  $\times$  512  $\times$  64 pixels, and the projected pixel size is 0.046  $\mu\text{m} \times 0.046 \mu\text{m} \times 0.050 \mu\text{m}$ . The PSF is commonly determined from images of subresolution microbeads by measuring spatial profiles of the fluorescence signal from individual microbeads and averaging the profile widths of multiple beads (Kozubek, 2001). We use a highly efficient alternative approach to determine the width of the PSF from multiple bead images. This method consists of two steps. First, the autocorrelation of the PSF is determined by

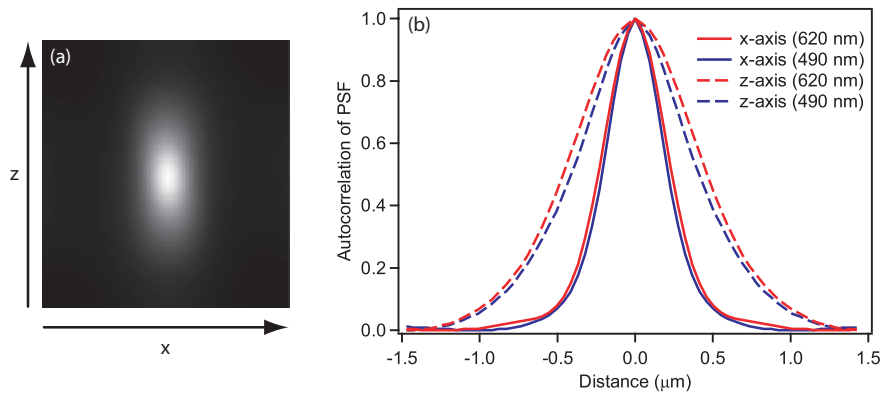


**Fig. 9.** (a)  $x$ - $z$  plane of the autocorrelation of the 3D point spread function. (b) Comparison of autocorrelation along the lateral ( $x$ -axis) and axial ( $z$ -axis) directions using fluorescence excitation wavelengths of 490 nm and 620 nm.

computing the 3D spatial autocorrelation of a confocal image containing multiple microbead images. Second, the width of the PSF is computed from the autocorrelation of the PSF. The 3D autocorrelation,  $A(x, y, z)$ , is defined as

$$A(x, y, z) = \sum_{i=0}^{L-1} \sum_{j=0}^{M-1} \sum_{k=0}^{N-1} S(i, j, k)S(i-x, j-y, k-z), \quad (4)$$

where  $S(i, j, k)$  is the signal at pixel  $i, j, k$  in the image of dimensions  $L, M, N$ . For computational efficiency, we perform the autocorrelation in the frequency domain using

$$A(x, y, z) = FFT^{-1}(|FFT(S(i, j, k))|^2), \quad (5)$$

where  $FFT$  and  $FFT^{-1}$  are the forward and inverse fast Fourier transforms, respectively. The dominant feature in the autocorrelation is the central peak, which corresponds to the self-correlation of the microbead images and is equivalent to the autocorrelation of the PSF. The correlation between different bead images produces weak secondary noise peaks in the autocorrelation. The magnitude of the secondary peaks is negligible compared to the self-correlation peak because the beads are randomly distributed in the confocal image and therefore the spacing between different beads is uncorrelated. If the confocal image of the beads has a relatively low signal-to-noise ratio (SNR), there is also a noise peak at the centre of the self-correlation peak that corresponds to the self-correlation of the noise. The magnitude of this noise peak has been minimized by increasing the SNR of the confocal image with longer pixel dwell times and averaging of multiple scans.

Figure 9a shows the  $x$ - $z$  plane from a central slice of the autocorrelation using 490-nm excitation. The autocorrelation is elongated in the axial direction ( $z$ -axis). The autocorrelation profiles along the lateral and axial directions are shown in Fig. 9b for the blue and red fluorescent microbeads. The autocorrelation is inherently broader than the PSF, and the width of the PSF is estimated from the autocorrelation function using a scaling relationship from ideal imaging optics. For ideal

**Table 1.** Point spread function FWHM.

$\lambda_{\text{excitation}}$ (nm)	Lateral	Axial
490	0.33 $\mu\text{m}$	0.68 $\mu\text{m}$
620	0.36 $\mu\text{m}$	0.77 $\mu\text{m}$

diffraction-limited lenses with a circular aperture, the PSF is an airy disk. The full width at half maximum (FWHM) of the airy disk is approximately a factor of 0.76 times smaller than the FWHM of the autocorrelation of the airy disk. We estimate the width of the PSFs by multiplying the FWHM of the measured autocorrelations by 0.76. Table 1 shows the PSF widths for the  $x$  and  $z$  axes for 490-nm and 620-nm fluorescence excitation. The axial PSF widths are approximately a factor of two larger than the lateral PSF widths. In both the axial and lateral dimensions, the FWHM at 620 nm is 10–15% larger than at 490 nm. We expect that the measured FWHM values are a conservative estimate of the actual PSF widths that would be measured using an ideal point source because the size of the microbeads is significant compared to the FWHM values (Kozubek, 2001).

The results of the PSF measurements indicate that chromatic aberrations are not a significant limitation for highly resolved multispectral confocal imaging throughout the visible spectrum and underline the excellent suitability of PCF-generated supercontinua for confocal microscopy applications. For further verification, we quantified the longitudinal chromatic aberrations by measuring the displacement along the  $z$ -axis that was introduced by imaging at different wavelengths. In these measurements, the reflection from a glass coverslip was detected as the position of the coverslip was scanned along the  $z$ -axis. At each wavelength, the optimal focus was defined as the  $z$ -position with the maximum signal from the coverslip. The results showed that the axial location of the focus varied by  $\pm 0.30 \mu\text{m}$  for illumination wavelengths between 470 nm and 650 nm.

This displacement is comparable to the FWHM of the PSF in Table 1. We conclude that longitudinal chromatic aberrations and chromatic variations in beam divergence are not a significant limitation to this multispectral confocal microscope system. This result offers exciting opportunities for applications that require precisely overlapped illumination at different wavelengths, such as fluorescence colocalization studies (Manders *et al.*, 1993; Bolte & Cordeliers, 2006), fluorescence resonance energy transfer (FRET), fluorescence cross-correlation microscopy and coherent anti-Stokes Raman scattering (CARS) microscopy. The complete control over laser intensity and wavelength also makes this instrument ideal for photoactivation experiments.

#### Spectrofluorometric confocal imaging of plants

Highly resolved spectrofluorometric confocal imaging is a powerful tool for a broad range of microscopy applications. As an illustration of this capability, we have performed fluorescence excitation scans with both 2D and 3D confocal imaging of a thin section of the rhizome of *Convallaria Majalis* (lily-of-the-valley) that was stained with safranin and fast green dyes. A complete 2D fluorescence excitation scan from 480 to 640 nm is available online (see *Convallaria* movie). Figures 10a and b show sample 2D fluorescence measurements of *Convallaria* at excitation wavelengths of 620 nm and 530 nm, respectively, corresponding to the peak excitation wavelengths of fast green and safranin (Li *et al.*, 2002; Angeles *et al.*, 2004). The fluorescence image at each excitation wavelength highlights different structures because the fast green and safranin dyes have affinities for different parts of the sample. In Fig. 10a, fluorescence signals from fast green are observed in many different regions of the rhizome. There is a thickened endodermis, which delimits the wide cortex from the pith. In the pith, there are scattered vascular bundles that contain xylem and phloem (Bowes, 1999).

To demonstrate that fluorescence excitation properties can be used to distinguish different structures, we consider four subregions of the image in Fig 10a, and show the corresponding excitation spectra for these structures in Fig 10c. Region 1 is part of the endodermis. Region 2 contains phloem, and regions 3 and 4 are different regions of xylem. In the excitation spectra, the narrower peak at 620 nm corresponds to fast green absorption (Li *et al.*, 2002) and occurs in all regions (Johansen, 1940). The broader spectral peak that spans 510–530 nm is absorption by safranin (Angeles *et al.*, 2004), and is only significant for regions 1 and 3. The endodermis and xylem contain lignin, which is stained by the safranin dye. Note that region 4, which contains xylem, shows negligible safranin absorption, indicating that there is differential staining of safranin in different parts of the xylem, as is evident in Fig. 10b. These spectrally resolved

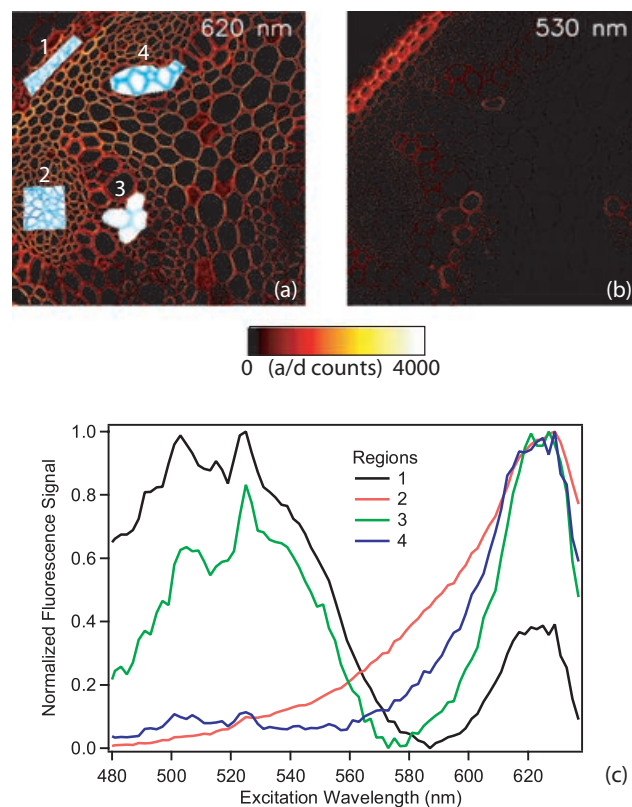
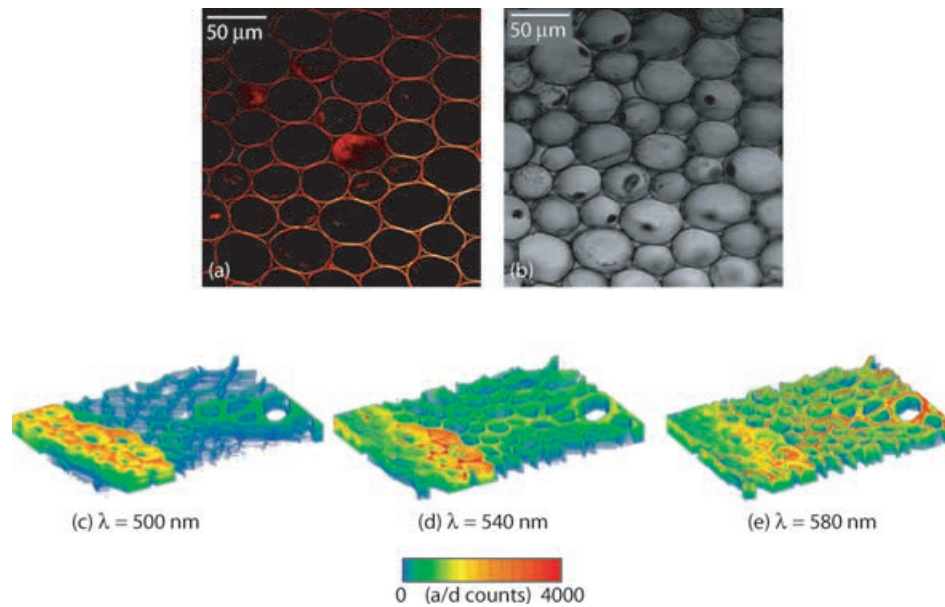


Fig. 10. (a, b) Two-dimensional confocal fluorescence images of *Convallaria* (lily-of-the-valley) rhizome with excitation at 620 nm and 530 nm for peak excitation of fast green and safranin, respectively. Image is  $355 \mu\text{m} \times 355 \mu\text{m}$ . Regions in (a) correspond to (1) endodermis, (2) phloem and (3, 4) xylem. (c) Fluorescence excitation spectra of the four regions of interest.

fluorescence measurements enable feature identification by providing a high degree of labelling specificity.

It is important that the integrated multispectral confocal microscope system retains the full functionality of the original confocal microscope. As a demonstration of the resolution capabilities of our modified CLSM system, high-resolution fluorescence and broadband transmission images of *Convallaria* are shown in Figs. 11a and b, respectively. These images resolve the detailed structure of the *Convallaria* cell walls, indicating excellent spatial resolution.

As a second demonstration of the CLSM capabilities, we performed 3D confocal imaging using different fluorescence excitation wavelengths. Figures 11c–e displays sample 3D fluorescence images that were measured with excitation wavelengths of 500 nm, 540 nm and 580 nm, respectively. The image dimensions are  $300 \times 200 \times 26$  voxels with each voxel corresponding to  $0.46 \times 0.46 \times 0.70 \mu\text{m}^3$ . These images show the detailed 3D structure of the *Convallaria* with preferential labelling of different structures with different excitation wavelengths, as described above for the 2D images in Fig. 10.



**Fig. 11.** High-resolution confocal (a) fluorescence and (b) broadband transmission images of *Convallaria* rhizome. The colour scale for (a) is the same as in Figs. 10a, b. (c–e) Comparison of 3D confocal fluorescence measurements of *Convallaria* with excitation wavelengths at 500, 540 and 580 nm. The imaged volume is  $92\ \mu\text{m} \times 138\ \mu\text{m} \times 18\ \mu\text{m}$ .

#### Spectrofluorometric confocal imaging of live cells

Spectrofluorometric imaging measurements are particularly powerful when applied to studies of living cells. Live-cell imaging requires that spectral scans are performed on a relatively fast timescale. As a demonstration of this capability, we performed a fluorescence excitation scan of live human U2OS Osteosarcoma cells that were transiently transfected with a plasmid expressing an mCherry-Rad51 fusion protein. Rad51 is a DNA-binding protein that is involved in DNA repair. The fluorescence excitation scan was measured from 537 to 607 nm using 2D confocal imaging. Figures 12a–c display sample images of a live cell using excitation wavelengths of 572, 587 and 602 nm. In the nucleus, distinctive entangled filament structures are produced by the overexpressed mCherry-Rad51 fusion protein forming fibrils around strands of DNA. In contrast, the cytoplasm shows regions of relatively homogeneous fluorescence signal as well as regions interspersed with aggregates (Pellegrini *et al.*, 2002). There are no fibrils in the cytoplasm due to the absence of DNA.

The full fluorescence excitation scan (see live-cell movie) was performed with 5-nm wavelength increments at a resolution of  $512 \times 512$  pixels with a two-frame Kalman filter at an average rate of 8.0 s/frame. The time required for confocal scanning and acquisition of a single frame was 5.4 s. The remaining 2.6 s for each frame was consumed by triggering the confocal microscope electronics, stepping the excitation wavelength and measuring the laser power. Further optimization of the integrated microscope system will enable increased frame rates.

mCherry is widely accepted as the best available genetically encoded monomeric fluorescent reporter protein in the red spectral range (Shaner *et al.*, 2005). The development of such a monomeric red fluorophore that is suitable for live-cell imaging of protein–protein interactions is important for three main reasons: multiplexing with other green fluorescent protein (GFP)-tagged proteins in localization studies, providing a cross-correlation pair for GFP and an acceptor FRET pair for Venus/yellow fluorescent protein (YFP). Previously, one of the main problems with mCherry was its relatively poor brightness as compared to GFP. The brightness,  $\epsilon$ , of a fluorescent protein is defined as the product of its extinction coefficient and quantum yield. The literature value for the brightness of mCherry is  $16\ (\text{mMcm})^{-1}$ , which is significantly lower than the brightness of extended yellow fluorescent protein (EYFP) ( $\epsilon = 51$ ) or extended green fluorescent protein (EGFP) ( $\epsilon = 34$ ; Shaner *et al.*, 2005).

In standard commercial microscopes, the detection sensitivity for mCherry is further degraded by the lack of optimal excitation sources. The peak excitation wavelengths for EGFP and EYFP are approximately 488 nm and 514 nm, respectively, and optimal excitation is accessible with an Ar-ion laser. Figure 12d shows the measured excitation spectrum of mCherry within a subregion of the cell in Figs. 12a–c. The peak excitation wavelength for mCherry is at 590 nm. For the commercial FluoView system, the nearest laser wavelengths that are available for excitation are the He-Ne laser at 543 nm and 633 nm and the Kr-ion laser at 568 nm. For some commercial systems, the Kr-ion laser is not available, and the nearest wavelengths are the He-Ne laser lines. The spectrum

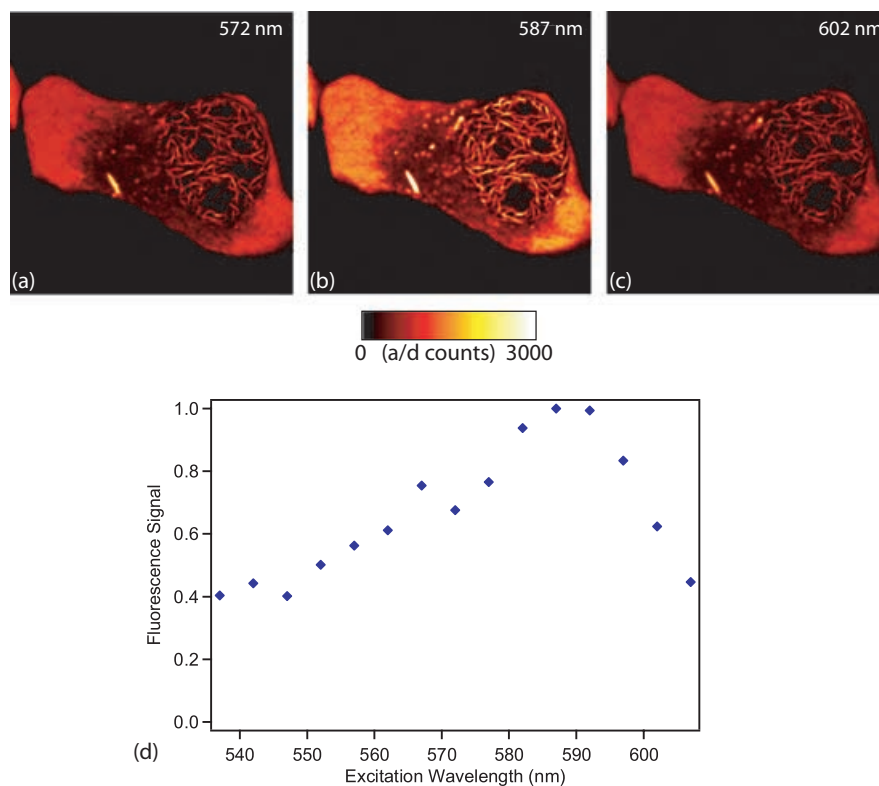


**Fig. 12.** (a–c) Confocal images from a fluorescence excitation scan of a human U2OS Osteosarcoma cell transfected with an mCherry-Rad51 fluorescent protein expressing construct. Image dimensions are  $59 \mu\text{m} \times 59 \mu\text{m}$ . Excitation wavelengths are indicated in each image. (d) Normalized fluorescence excitation spectrum of mCherry-Rad51 from a region within the cytoplasm.

in Fig. 12d shows that excitation with these fixed laser lines provides significantly lower sensitivity than excitation at 590 nm. For example, excitation of mCherry with a He-Ne laser at 543 nm is 60% less efficient than excitation at 590 nm. The supercontinuum laser provides access to the peak excitation wavelength of approximately 590 nm, thus enabling optimum detection sensitivity.

This ability to perform *in situ* fluorescence excitation scans provides important insight into fluorophore properties in cell environments. For example, protein aggregation and association of proteins to cellular substructures may result in subtle spectral shifts that would be impossible to detect with fixed wavelength systems. The absorption spectrum of mCherry is known to shift with changing pH (Shu *et al.*, 2006). Fluorescence excitation scans with the supercontinuum laser can be used to detect these shifts.

## Conclusions

We have demonstrated spectrofluorometric confocal imaging using a supercontinuum fibre laser and a prism spectrometer and have fully integrated these systems with a commercial confocal microscope. With simple adaptations, the methodology described here permits any existing fixed wavelength confocal system to be converted into a platform

that provides diffraction-limited spectrofluorometric imaging capabilities. The system is compact, economical and turn-key, without affecting the inherent functionality of the confocal microscope. High-resolution fluorescence imaging is feasible throughout the visible spectrum with relatively minor effects of chromatic aberration. Different excitation wavelengths exhibit excellent parfocality without the need for inserting corrective optics into the beam path after the collimating optics from the supercontinuum laser source. Corrections for variations in excitation laser power are performed on a frame-by-frame basis, which is important for quantitative measurements over a wide range of wavelengths. Spectral imaging capabilities are sufficiently fast to track dynamic phenomena in living cells and can be improved using parallel detection arrays. The system facilitates multiplexed measurements of different fluorophores and can improve contrast between fluorescent labels and autofluorescence. This new capability may enable the use of autofluorescence signatures as a diagnostic tool.

Spectrofluorometric imaging can significantly enhance the sensitivity of fluorescence measurements by enabling optimal excitation and detection of fluorophores. For example, FRET measurements could be improved by minimizing spectral bleed-through and cross-talk (Elangovan *et al.*, 2003). It is expected that supercontinuum sources will replace traditional

fixed-wavelength lasers in many microscopy applications, and with full spectral capabilities in confocal microscopy, biophysical research is entering a new era.

### Acknowledgments

This work was supported by grants from the Royal Society, the Engineering and Physical Sciences Research Council (EPSRC), and the Higher Education Funding Council for England (HEFCE). J.H. Frank and C.F. Kaminski acknowledge support by a PLATFORM grant from the EPSRC. J.H. Frank acknowledges support by the U.S. Department of Energy, Office of Basic Energy Sciences, Division of Chemical Sciences, Geosciences, and Biosciences. Sandia National Laboratories is a multiprogram laboratory operated by Sandia Corporation, a Lockheed Martin Company, for the U.S. Department of Energy under contract DE-AC04-94-AL85000. C.F. Kaminski is grateful to the Leverhulme Trust for personal sponsorship.

### References

- Angeles, G., Owens, S.A. & Ewers, F.W. (2004) Fluorescence shell: a novel view of sclereid morphology with the confocal laser scanning microscope. *Microsc. Res. Tech.* **63**, 282–288.
- Betz, T., Teipel, J., Koch, D., Hartig, W., Guck, J., Kas, J. & Giessen, H. (2005) Excitation beyond the monochromatic laser limit: simultaneous 3-D confocal and multiphoton microscopy with a tapered fiber as white-light laser source. *J. Biomed. Opt.* **10**, 54009–1–7.
- Betzig, E., Patterson, G.H., Sougrat, R., *et al.* (2006) Imaging intracellular fluorescent proteins at nanometer resolution. *Science* **313**, 1642–1645.
- Bolte, S. & Cordelières, F.P. (2006) A guided tour into subcellular colocalization analysis in light microscopy. *J. Microsc.* **224**, 213–232.
- Borlinghaus, R., Gugel, H., Albertano, P. & Seyfried, V. (2006) Closing the spectral gap: the transition from fixed-parameter fluorescence to tunable devices in confocal microscopy. *Proc. SPIE* **6090**, 60900T–1–6.
- Born, M. & Wolf, E. (1980) *Principles of Optics*, Pergamon Press, New York.
- Bowes, B.G. (1999) *A Color Atlas of Plant Structure*, Manson Publishing, London.
- Denk, W., Piston, D.W. & Webb, W.W. (1995) Two-photon molecular excitation in laser-scanning microscopy. *Handbook of Biological Confocal Microscopy* (ed. J. B. Pawley). 2nd ed. Plenum Press, New York.
- Diaspro, A., Chirico, G., Federici, F., Cannone, E., Beretta, S. & Robello, M. (2001) Two-photon microscopy and spectroscopy based on a compact confocal scanning head. *J. Biomed. Opt.* **6**, 300–310.
- Dudley, J.M., Genty, G. & Coen, S. (2006) Supercontinuum generation in photonic crystal fiber. *Rev. Mod. Phys.* **78**, 1135–1184.
- Dunsby, C., Lanigan, P.M.P., McGinty, J., *et al.* (2004) An electronically tunable ultrafast laser source applied to fluorescence imaging and fluorescence lifetime imaging microscopy. *J. Phys. D: Appl. Phys.* **37**, 3296–3303.
- Elangovan, M., Wallrabe, H., Chen, Y., Day, R.N., Barroso, M. & Periasamy, A. (2003) Characterization of one- and two-photon excitation fluorescence resonance energy transfer microscopy. *Methods* **29**, 58–73.
- Frederix, P., Asselbergs, M.A.H., Van Sark, W., Van Den Heuvel, D.J., Hamelink, W., De Beer, E.L. & Gerritsen, H.C. (2001) High sensitivity spectrograph for use in fluorescence microscopy. *Appl. Spectrosc.* **55**, 1005–1012.
- Johansen, D.A. (1940) *Plant Microtechnique*, McGraw-Hill, New York.
- Klein, M.V. & Furtak, T.E. (1986) *Optics*, Wiley, New York.
- König, K. (2000) Multiphoton microscopy in life sciences. *J. Microsc.* **200**, 83–104.
- Kozubek, M. (2001) Theoretical versus experimental resolution in optical microscopy. *Microsc. Res. Tech.* **53**, 157–166.
- Li, Y.F., Huang, C.Z. & Li, M. (2002) A resonance light-scattering determination of proteins with fast green FCF. *Anal. Sci.* **18**, 177–181.
- Lippincott-Schwartz, J., Altan-Bonnet, N. & Patterson, G.H. (2003) Photobleaching and photoactivation: following protein dynamics in living cells. *Nat. Cell Biol.* **S7–S14**.
- Luong, A.K., Gradinaru, G.C., Chandler, D.W. & Hayden, C.C. (2005) Simultaneous time- and wavelength-resolved fluorescence microscopy of single molecules. *J. Phys. Chem. B* **109**, 15691–15698.
- Manders, E.M.M., Verbeek, F.J. & Aten, J.A. (1993) Measurement of colocalization of objects in dual-color confocal images. *J. Microsc.* **169**, 375–382.
- McConnell, G. (2004) Confocal laser scanning fluorescence microscopy with a visible continuum source. *Opt. Express* **12**, 2844–2850.
- Palero, J.A., Boer, V.O., Vijverberg, J.C., Gerritsen, H.C. & Sterenborg, H. (2005) Short-wavelength two-photon excitation fluorescence microscopy of tryptophan with a photonic crystal fiber based light source. *Opt. Express* **13**, 5363–5368.
- Pawley, J.B. (1995) *Handbook of Biological Confocal Microscopy*, Plenum Press, New York.
- Pellegrini, L., Yu, D.S., Lo, T., Anand, S., Lee, M., Blundell, T.L. & Venkitaraman, A.R. (2002) Insights into DNA recombination from the structure of a RAD51-BRCA2 complex. *Nature* **420**, 287–293.
- Plessow, R., Brockhinke, A., Eimer, W. & Kohse-Hoinghaus, K. (2000) Intrinsic time- and wavelength-resolved fluorescence of oligonucleotides: a systematic investigation using a novel picosecond laser approach. *J. Phys. Chem. B* **104**, 3695–3704.
- SCHOTT (2006) Available at: [http://www.us.schott.com/optics\\_devices/english/products/flash/abbediagramm\\_flash.html](http://www.us.schott.com/optics_devices/english/products/flash/abbediagramm_flash.html). Accessed 15 September 2006
- Schultz, R.A., Nielsen, T., Zavaleta, J.R., Ruch, R., Wyatt, R. & Garner, H.R. (2001) Hyperspectral imaging: a novel approach for microscopic analysis. *Cytometry* **43**, 239–247.
- Shaner, N.C., Steinbach, P.A. & Tsien, R.Y. (2005) A guide to choosing fluorescent proteins. *Nat. Methods* **2**, 905–909.
- Shu, X.K., Shaner, N.C., Yarbrough, C.A., Tsien, R.Y. & Remington, S.J. (2006) Novel chromophores and buried charges control color in mFruits. *Biochemistry* **45**, 9639–9647.
- Sinclair, M.B., Haaland, D.M., Timlin, J.A. & Jones, H.D.T. (2006) Hyperspectral confocal microscope. *Appl. Opt.* **45**, 6283–6291.
- Stephens, D.J., Lin-Marq, N., Pagano, A., Pepperkok, R. & Paccaud, J.P. (2000) COPI-coated ER-to-Golgi transport complexes segregate from COPII in close proximity to ER exit sites. *J. Cell Sci.* **113**, 2177–2185.
- Tadrous, P.J., Siegel, J., French, P.M.W., Shousha, S., Lalani, E.N. & Stamp, G.W.H. (2003) Fluorescence lifetime imaging of unstained tissues: early results in human breast cancer. *J. Pathol.* **199**, 309–317.
- Zellweger, M., Grosjean, P., Goujon, D., Monnier, P., Van Den Bergh, H. & Wagnieres, G. (2001) In vivo autofluorescence spectroscopy of human

bronchial tissue to optimize the detection and imaging of early cancers.  
*J. Biomed. Opt.* **6**, 41–51.

Zimmermann, T., Rietdorf, J. & Pepperkok, R. (2003) Spectral imaging and its applications in live cell microscopy. *FEBS Lett.* **546**, 87–92.

### Supplementary Material

The following supplementary material is available for this article:

**Video Clip S1.** Convallaria movie for Figure 10;

**Video Clip S2.** Live Cell movie for Figure 12.

This material is available as part of the online article from:  
<http://www.blackwell-synergy.com/doi/10.1111/j.1365-2818.2007.01803.x>

(This link will take you to the article abstract)

Please note: Blackwell Publishing are not responsible for the content or functionality of any supplementary materials supplied by the authors. Any queries (other than missing material) should be directed to the corresponding author for the article.